Article

Dual-functional dielectric metasurface doublets

Kai Bian , Daquan Lu * and Wei Hu *

Guangdong Provincial Key Laboratory of Nanophotonic Functional Materials and Devices, South China Normal University, Guangzhou 510631, China; biankai1314@163.com (K.B.); ludq@scnu.edu.cn (D.L.); huwei@scnu.edu.cn (W.H.)

* Correspondence: ludq@scnu.edu.cn (D.L.); huwei@scnu.edu.cn (W.H.)

Abstract: Based on the principle of Pancharatnam-Berry phase, we propose an approach to construct dual-functional dielectric metasurface doublets. This type of doublet, which is composed of a substrate and two metasurface layers, performs two different functionalities at two different operating wavelengths. The simulated results of the examples show that the designed dual-functional doublet works well as expected. The proposed approach can be used to design dielectric meta-structures with more layers of meta-surface and thereby with more functionalities, and would be of interest for miniaturization and integration.

Keywords: metasurface; Pancharatnam-Berry phase; dual-functionality

1. Introduction

In recent years, metasurfaces have aroused considerable interest for their ability of manipulating light by altering the amplitude, phase, and polarization states through sub-wavelength structures [1–13]. It has been demonstrated that metasurfaces can be utilized in various applications such as wave retarders [14], beam splitters [15], beam generators [16–23], metalenses [24–35], holograms [36–38], and nonlinear devices [39,40]. In addition, because metasurfaces can be much thinner than the conventional bulky optical components, they are of interest for the miniaturization and integration. In regard to the application of metasurfaces in integration, a natural question is, can a metasurface device be multifunctional? The answer is yes. In fact, in recent years much effort has been put to search for the multifunctional metasurface structures. It has been revealed that the multifunctional metasurface devices can be constructed through different approaches, such as the vertical stacking of multiple metallic metasurfaces [41], the in-plane spatial multiplexing in a single-layer metasurface [42–45], the dispersion engineering of phase shifters [46], and the hybrid design of propagation phase and geometric phase [47,48].

In this paper, we apply the vertical stacking method to the dielectric metasurfaces and propose an approach to construct dual-functional dielectric metasurface doublets, on the basis of the principle of Pancharatnam-Berry (PB) phase. The doublet, which is composed of a substrate and two metasurface layers, performs two different functionalities at two different wavelengths. To find the expected meta-structure, the three-dimensional finite-difference time-domain (FDTD) method is utilized to optimize the geometric parameters of the nanofins in the two metasurface layers. The simulation results show that, for one operating wavelength, the upper layer acts as a half-wave plate, and the lower layer acts as a full-wave plate. And it is just the opposite for the other operating wavelength. Therefore, for each operating wavelength, the PB phase distribution and thereby the functionality can be designed by adjusting the orientation angle of the nonofins in the corresponding layer which acts as a half-wave plate. We also illustrate two examples to show the performance of the designed dual-functional doublet. The simulated results show that it works well as expected.

2. Design and optimization

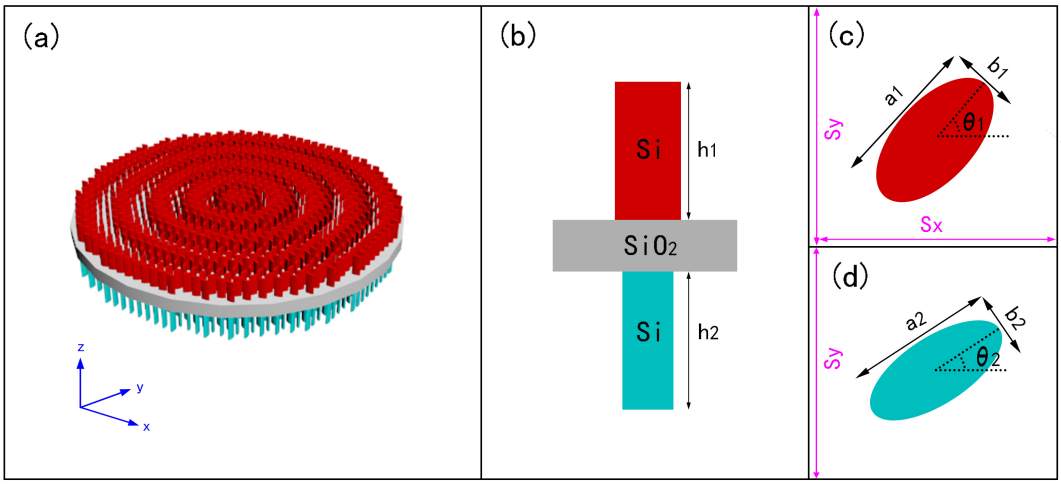

Figure 1. (a) Schematic diagram of the dual-functional metasurface doublet, which comprises two layers of elliptical amorphous silicon nanofins patterned on both sides of a glass substrate. (b) Side view of the unit cell. (c) Top view of the unit cell for the top layer of metasurface. (d) Top view of the unit cell for the lower layer of metasurface. Geometric parameters of each unit cell are shown in (b-d).

Figure 1 shows the schematic diagram of the designed dual-functional metasurface doublet, of which the two working wavelengths are λ_1 and λ_2. As shown in Figure 1a, the metasurface doublet comprises two layers of elliptical amorphous silicon nanofins patterned on both sides of a glass substrate. The upper (bottom) layer of the doublet consists of amorphous silicon elliptical nanofins with the same major axis a_1 (a_2), minor axis b_1 (b_2), and height h_1 (h_2) but different rotation angles θ_1 (θ_2). Figure 1b-d present a unit cell which is composed of two amorphous silicon elliptical nanofins with high refractive index and low loss sitting on the upper and lower sides of a fused-silica substrate.

It is well-known that, for a circularly polarized incident light with a specific wavelength, the nanofins which function as full-wave plates have no effect on the phase distribution of the light field. However, the nanofins function as half-wave plates would convert a circularly polarized incident light into the transmitted light with opposite helicity and produce the so-called Pancharatnam-Berry phase: $\varphi(x,y) = 2\theta(x,y)$. Therefore, one can impart the required phase distribution $\varphi(x,y)$ by rotating the orientation angle of the nanofins, i.e., $\theta(x,y)$.

To construct the dual-functional metasurface doublet, the geometric parameters of each unit cell should be properly selected so that, for the incident wavelength λ_1 (λ_2), each nanofin in the upper layer of metasurface functions as a half-wave plate (full-wave plate), and each nanofin in the lower layer of metasurface functions as a full-wave plate (half-wave plate). In this case, the phase distributions of λ_1 and λ_2 can be independently controlled by the upper and lower layers of metasurface, respectively. In this way, the metasurface doublet becomes dual-functional, and the functionalities can be switched by simply changing the incident wavelength.

In order to find the expected meta-structure, we utilize the three-dimensional FDTD method to optimize the geometric parameters of the nanofins. For the example shown in Figure 2a, b, the size of each unit cell is $s_x \times s_y = 300nm \times 300nm$, the nanofins are assumed to be elliptic cylindrical, the operating wavelengths are assumed to be $\lambda_1 = 780nm$ and $\lambda_2 = 660nm$, and the heights of the nonofins in the two layers are $h_1 = 600nm$ and $h_2 = 800nm$. To construct the nanofins which function as half-wave plates for one operating wavelength and function as full-wave plates for the other, the major and minor axes of the elliptic nanofins should be optimized first.

In Figure 2a, b, we change the lengths of the major and minor axes and get the phase difference, i.e., the difference between the phase shift of a light linearly polarized along the major axis ($\varphi_x^{(1,2)}$) and that along the minor axis ($\varphi_y^{(1,2)}$),

$$\triangle\varphi^{(1,2)} = |\varphi_x^{(1,2)} - \varphi_y^{(1,2)}|. \quad (1)$$

In the simulation, the spatial mesh grids are set as $\triangle x = \triangle y = \triangle z = 10nm$. The perfectly matched layer (PML) boundary condition is used along the z axis and the periodic boundary condition is applied along the x and y axes.

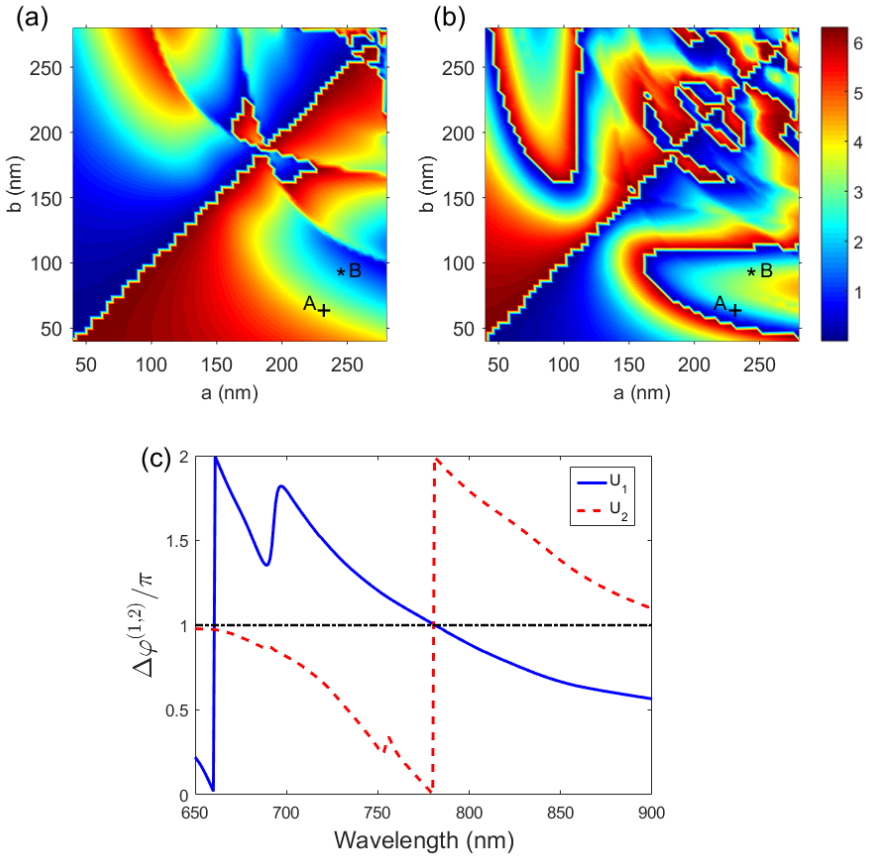

Figure 2. (a) The phase difference ($\triangle\varphi^{(1)}$) of each elliptical nanofin in the upper layer for different lengths of major and minor axes. The wavelength is $\lambda_1 = 780nm$. (b) The phase difference ($\triangle\varphi^{(2)}$) of each elliptical nanofin in the lower layer for different lengths of major and minor axes. The wavelength is $\lambda_2 = 660nm$. (c) The phase difference as a function of the wavelength for U_1 and U_2 .

By filtering the data shown in Figure 2a, b, we find that, at the point A ($a_1 = 238nm$, $b_1 = 70nm$, $h_1 = 600nm$, the corresponding unit cell is defined as U_1), the phase difference $\triangle\varphi^{(1)}$ approximates well to π for $\lambda_1 = 780nm$, and approximates well to zero for $\lambda_2 = 660nm$. Meanwhile, at the point B ($a_2 = 248nm$, $b_2 = 94nm$, $h_2 = 800nm$, the corresponding unit cell is defined as U_2), the phase difference $\triangle\varphi^{(2)}$ approximates well to π for $\lambda_2 = 660nm$, and approximates well to zero for $\lambda_1 = 780nm$. In addition, in Figure 2c we illustrate the phase differences for U_1 and U_2 at a broadband spectrum of $650 - 900nm$. The results further verify that U_1 (U_2) can be regarded as a half-wave plate (full-wave plate) for $\lambda_1 = 780nm$ and a full-wave plate (half-wave plate) for $\lambda_2 = 660nm$. Therefore, we can construct a dual-functional doublet (of which the unit cell is defined as U_1+U_2) by patterning the two metasurface layers (of which the unit cells are U_1 and U_2, respectively) on both sides of the substrate.

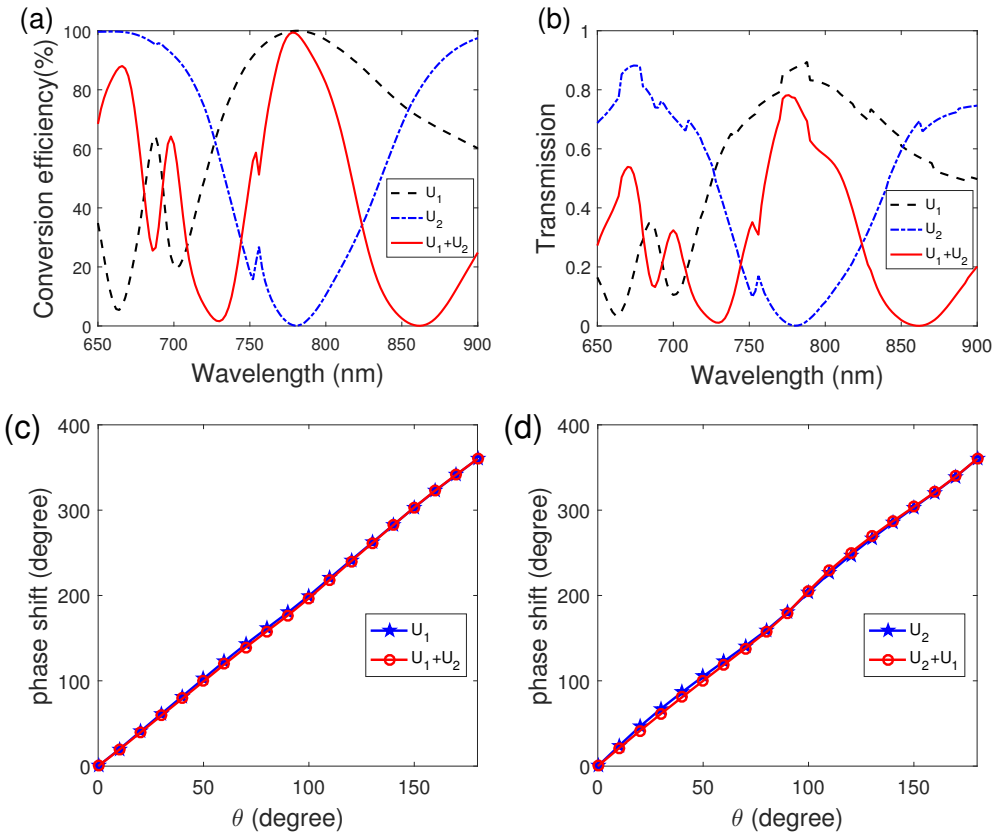

Figure 3. (a) Simulated polarization conversion efficiency for the single layer cases (U_1, U_2) and the doublet case ($U_1 + U_2$). (b) Simulated transmission for the single layer cases (U_1, U_2) and the doublet case ($U_1 + U_2$). (c) Comparison between the phase shift as a function of the rotation angle θ for the single-layer unit cell U_1 and that for the double-layer unit cell $U_1 + U_2$. The wavelength is $\lambda_1 = 780nm$. (d) The same as that in (c) except that the single-layer unit cell is U_2 and the wavelength is $\lambda_2 = 660nm$.

Figure 3a shows the polarization conversion efficiency (defined as the ratio of the energy of the cross-polarized light wave to that of the total transmitted light wave) for the single layer cases (U_1 and U_2) and the doublet case ($U_1 + U_2$). It is found that, for the doublet case, the polarization conversion efficiency arrives two peaks (99.5% and 85%) around the two designed operating wavelengths $\lambda_1 = 780nm$ and $\lambda_2 = 660nm$.

Figure 3b illustrates the transmission (defined as the ratio of the energy of the cross-polarized light wave to that of the total incident light wave) for the single layer cases (U_1, U_2) and the doublet case ($U_1 + U_2$). It can be observed that the unit cell U_1 has the highest transmission (about 0.9) around the wavelength of $780nm$, and the transmission at the wavelength of $660nm$ is close to 0. On the other hand, the transmission of the unit cell U_2 is the highest (about 0.88) around the wavelength of $660nm$ and approaches 0 at $780nm$. In the doublet case $U_1 + U_2$, although the transmission is lower than that in the single-layer cases, the transmission peaks also exist around the wavelengths $\lambda_1 = 780nm$ and $\lambda_2 = 660nm$.

Figure 3c, d illustrate the comparison of the simulated phase shift as a function of the rotation angle θ for the single layer case (U_1 or U_2) and that for the doublet case ($U_1 + U_2$). The result shows that, at the designed operating wavelengths $\lambda_1 = 780nm$ and $\lambda_2 = 660nm$, the phase shift for the doublet case is in good agreement with that for the single layer case. Detailedly speaking, the relation between the PB phase and the orientation angle of the nanofins, $\varphi(x, y) = 2\theta(x, y)$, is also satisfied for the doublet case. Therefore, we can reasonably estimate that the meta-structure doublet ($U_1 + U_2$) would work well at the designed operating wavelengths.

3. Examples

We introduce two examples to verify the performance of the proposed dual-functional structure in the following. First, as shown in Figure 4, we construct a dual-functional device which acts as a meta-axicon and a meta-lens at the wavelengths $\lambda_1 = 780nm$ and $\lambda_2 = 660nm$, respectively. For a planar meta-axicon to generate zero-order Bessel beam, the phase distribution satisfies

$$\varphi_{\lambda_1}(x,y) = 2\pi - \frac{2\pi}{\lambda_1} \cdot \sqrt{x^2+y^2} \cdot \mathrm{NA}, \tag{2}$$

where $\mathrm{NA} = \sin\alpha$ represents the numerical aperture. And a meta-lens for focusing requires that the phase distribution is

$$\varphi_{\lambda_2}(x,y) = \frac{2\pi}{\lambda_2}(f - \sqrt{x^2+y^2+f^2}), \tag{3}$$

where f is the preset focal length. The phase distributions φ_{λ_1} and φ_{λ_2} are obtained via rotating elliptical nanofins on both sides of the doublet according to the relation $\theta_{\lambda_1,\lambda_2}(x,y) = (1/2)\varphi_{\lambda_1,\lambda_2}(x,y)$.

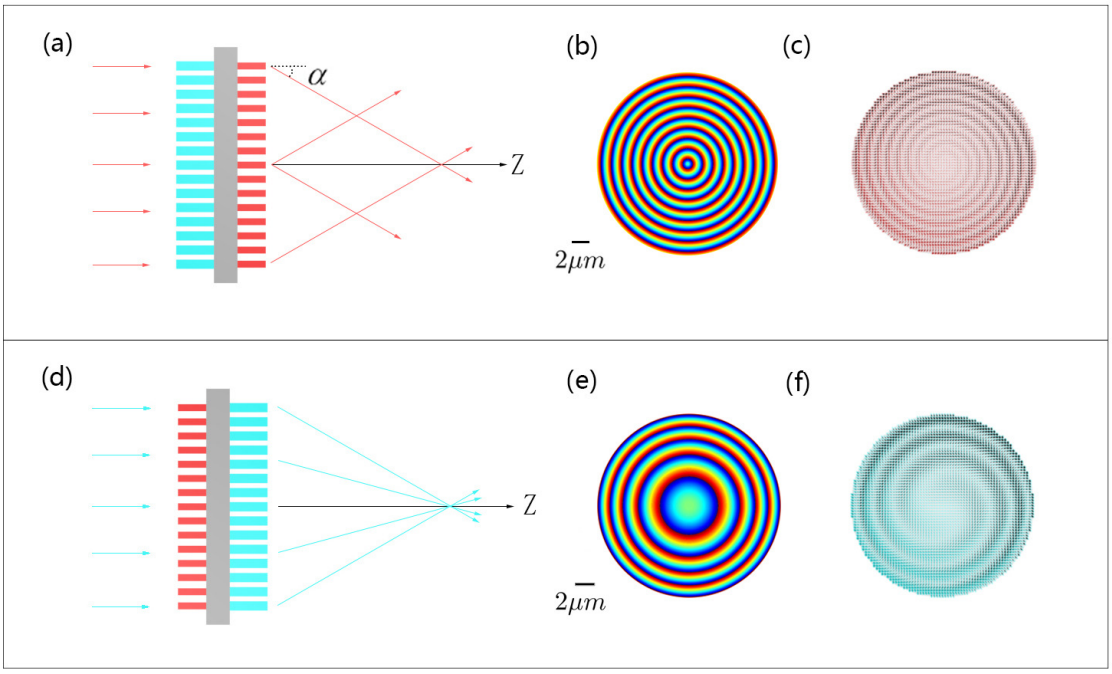

Figure 4. Design of a dual-functional device which acts as a meta-axicon and a meta-lens at the wavelengths $\lambda_1 = 780nm$ and $\lambda_2 = 660nm$, respectively. (a) Schematic diagram of a metal-axicon for generating a zero-order Bessel beam. (b) The required continuous phase distribution of the meta-axicon for NA=0.7. (c) The arrangement of elliptical amorphous silicon nanofins in the upper layer of metasurface in FDTD simulation. (d) Schematic diagram of a metal-lens for focusing. (e) The required continuous phase distribution of the meta-lens for $f = 15\mu m$. (f) the arrangement of elliptical silicon nanofins in the lower layer of metasurface in FDTD simulation.

When the incident plane wave is at the wavelength $\lambda_1 = 780nm$, the doublet acts as a meta-axicon and generates a zero-order Bessel beam (Figure 5). As expected, the intensity of the main lobe at the beam center is much stronger than that of the side lobes (Figure 5a, b). Moreover, the size of the main lobe remains almost the same within the maximum non-diffraction distance $Z_{max} = R/\tan[\arcsin(\mathrm{NA})] = 15.3\mu m$ (Figure 5b, c), where R is the radius of the aperture. The measured full width at half maximum (FWHM) of the main lobe is about 440nm(Figure 5c), which is very close to its theoretical limit ($= 0.358\lambda/\mathrm{NA} = 400nm$).

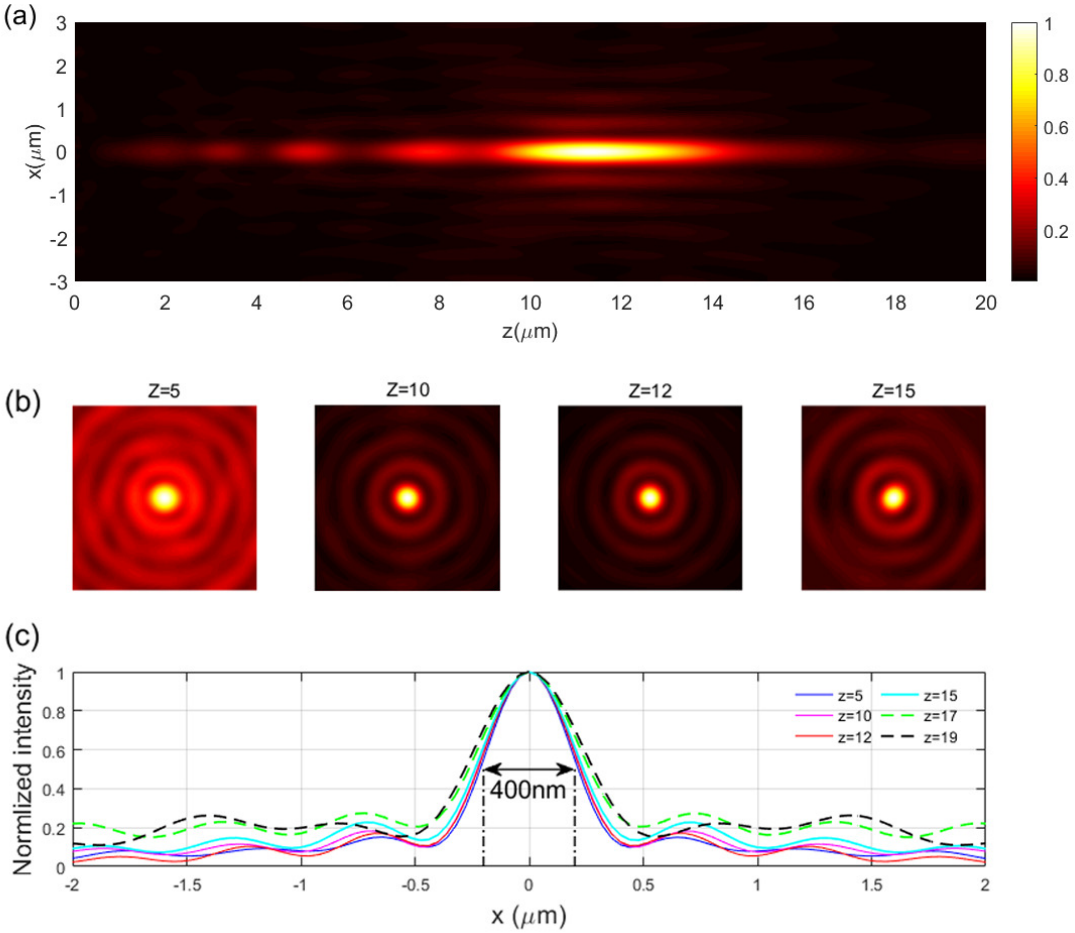

Figure 5. (a) Simulated normalized intensity profile in x-z plane when the wavelength is $\lambda_1 = 780nm$, at which the device acts as a meta-axicon with NA = 0.7. (b) The beam patterns at different propagation distances. (c) The transverse normalized intensity distributions at different propagation distances.

However, the doublet acts as a meta-lens when the incident plane wave is at the wavelength $\lambda_2 = 660nm$ (Figure 6). It provides strong focusing capability and focuses the beam at $z = 15.64\mu m$, which approximates well to the preset focusing location $z = 15.4\mu m$. The FWHM of the focal spot (480 nm) is very close to the diffraction limit ($= 0.5\lambda/\text{NA} = 467nm$). In addition, the FWHM of the beam increases quickly with the distance from the focus. These results demonstrate a good focusing performance of the doublet for $\lambda_2 = 660nm$.

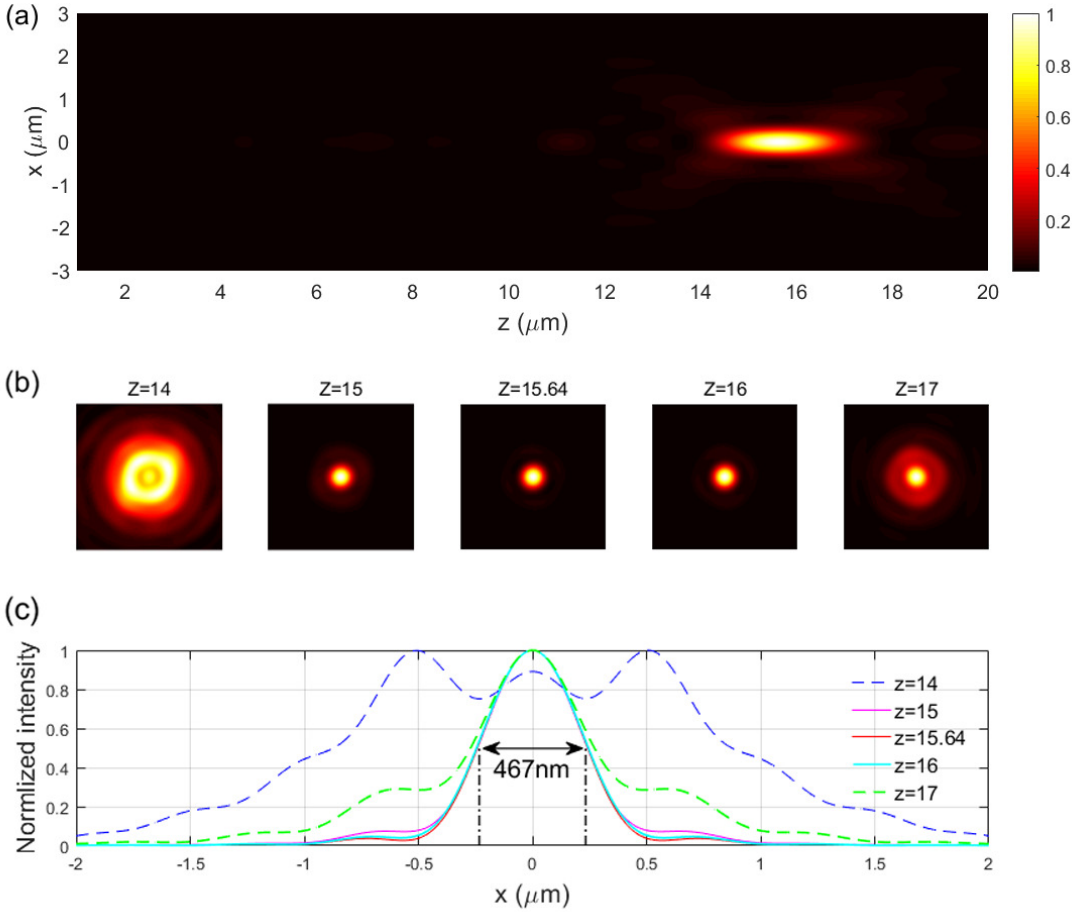

Figure 6. (a) Simulated normalized intensity profile in x-z plane when the wavelength is $\lambda_2 = 660nm$, at which the device acts as a meta-lens. (b) The beam patterns at different propagation distances. (c) The transverse normalized intensity distributions at different propagation distances.

The second example is a dual-pattern generator, which generates a (0, 1) and a (1, 0) mode Hermite-Gaussian focused pattern when the incident light is composed of two operating wavelengths: $\lambda_1 = 780nm$ and $\lambda_2 = 660nm$ (Figure 7a). The phase distribution for $\lambda_1 = 780nm$ and $\lambda_2 = 660nm$ are

$$\varphi_{\lambda_1}(x,y) = \begin{cases} \frac{2\pi}{\lambda_1}\left(f_1 - \sqrt{(x-x_1)^2 + (y-y_1)^2 + f_1^2}\right) & y > 0 \\ \frac{2\pi}{\lambda_1}\left(f_1 - \sqrt{(x-x_1)^2 + (y-y_1)^2 + f_1^2}\right) + \pi & y < 0 \end{cases} \tag{4}$$

and

$$\varphi_{\lambda_2}(x,y) = \begin{cases} \frac{2\pi}{\lambda_2}\left(f_2 - \sqrt{(x-x_2)^2 + (y-y_2)^2 + f_2^2}\right) & x > 0 \\ \frac{2\pi}{\lambda_2}\left(f_2 - \sqrt{(x-x_2)^2 + (y-y_2)^2 + f_2^2}\right) + \pi & x < 0 \end{cases} \tag{5}$$

respectively. Where (x_1, y_1, f_1) and (x_2, y_1, f_2) are the positions of the two generated patterns. Our simulation results show that, when the left-handed circularly polarized beam composed of the two operating wavelengths λ_1, λ_2 illuminates the designed metasurface doublet, the dual-pattern is generated as expected (Figure 7b).

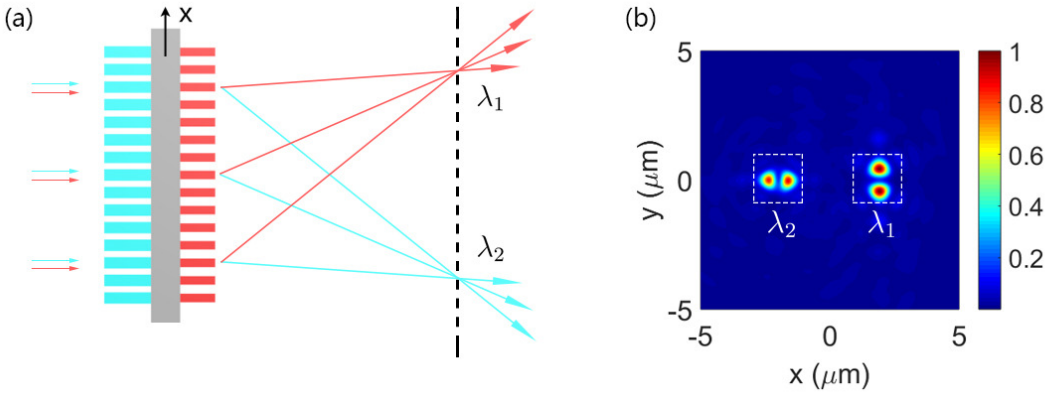

Figure 7. (a) Schematic diagram of the dual-pattern generator which generates a (0, 1) and a (1, 0) mode Hermite-Gaussian focused pattern when the incident light is composed of two wavelengths: $\lambda_1 = 780nm$ and $\lambda_2 = 660nm$. The values of other parameters are: $f_1 = f_2 = 15\mu m$, $x_1 = 2\mu m$, $x_2 = -2\mu m$, $y_1 = y_2 = 0$, $NA = 0.7$. (b) Simulated intensity distribution of the dual-pattern generated by the designed device.

4. Conclusion

In conclusion, the designed dielectric dual-functional doublet, which is composed of a substrate and two metasurface layers, performs two different functionalities at two different operating wavelengths. For one operating wavelength, the upper (lower) layer acts as a half-wave plate (full-wave plate), therefore the PB phase and thereby the functionality can be designed by adjusting the orientation angle of the nonofins in the upper layer. In a similar way, the functionality for the other operating wavelength can be designed by adjusting the orientation angle of the nonofins in the lower layer. It is verified by the examples that the designed dual-functional doublet works well as expected. The proposed approach can be used to design dielectric meta-structures with more layers of meta-surface and thereby with more functionalities, and would be of interest for miniaturization and integration.

Author Contributions: Conceptualization, K.B.; Methodology, K.B.; Software, K.B.; Validation, K.B. and D.L.; Formal Analysis, D.L. and K.B.; Investigation, K.B.; D.L. and W.H.; Data Curation, K.B.; Writing—Original Draft Preparation, K.B.; Writing—Review and Editing, D.L., W.H. and K.B.; Visualization, K.B.; Supervision, D.L.; Project Administration, D.L.; Funding Acquisition, D.L. and W.H.

Funding: This research was funded by the National Natural Science Foundation of China (Grants No. 11174090, No.11174091, and No. 61575068).

Conflicts of Interest: The authors declare no conflict of interest.

References

1. Yu, N.; Genevet, P.; Kats, M.A.; Aieta, F.; Tetienne, J.-P.; Capasso, F.; Gaburro, Z. Light Propagation with Phase Discontinuities: Generalized Laws of Reflection and Refraction. *Science* **2011**, *334*, 333–337.
2. Huang, L.; Chen, X.; Mühlenbernd, H.; Li, G.; Bai, B.; Tan, Q.; Jin, G.; Zentgraf, T.; Zhang, S. Dispersionless phase discontinuities for controlling light propagation[J]. *Nano Lett.* **2012**, *12*, 5750-5755.
3. Kildishev, A.V.; Boltasseva, A.; Shalaev, V.M. Planar photonics with metasurfaces. *Science* **2013**, *339*, 1232009.
4. Karimi, E.; Schulz, S.A.; De Leon, I.; Qassim, H.; Upham, J.; Boyd, R.W. Generating optical orbital angular momentum at visible wavelengths using a plasmonic metasurface. *Light: Sci. Appl.* **2014**, *3*, e167.
5. Kim, S.W.; Yee, K.J.; Abashin, M.; Pang, L.; Fainman, Y. Composite dielectric metasurfaces for phase control of vector field. *Opt. Lett.* **2015**, *40*, 2453-2456.
6. Li, G.; Kang, M.; Chen, S.; Zhang, S.; Pun, E.Y.B.; Cheah, K.W.; Li, J. Spin-enabled plasmonic metasurfaces for manipulating orbital angular momentum of light. *Nano Lett.* **2013**, *13*, 4148-4151.
7. Sun, S.; Yang, K.Y.; Wang, C.M.; Juan, T.K.; Chen, W.T.; Liao, C.Y.; He, Q.; Xiao, S.Y.; Kung, W.T.; Guo, G.Y.; Zhou, L. High-efficiency broadband anomalous reflection by gradient meta-surfaces. *Nano Lett.* **2012**, *12*, 6223-6229.

8. Bouchard, F.; De Leon, I.; Schulz, S.A.; Upham, J.; Karimi, E.; Boyd, R.W. Optical spin-to-orbital angular momentum conversion in ultra-thin metasurfaces with arbitrary topological charges. *Appl. Phys. Lett.* **2014**, *105*, 101905.
9. Yin, X.; Ye, Z.; Rho, J.; Wang, Y.; Zhang, X. Photonic spin Hall effect at metasurfaces. *Science* **2013**, *339*, 1405-1407.
10. Chen, W.T.; Török, P.; Foreman, M.R.; Liao, C.Y.; Tsai, W.Y.; Wu, P.R.; Tsai, D.P. Integrated plasmonic metasurfaces for spectropolarimetry. *Nanotechnology* **2016**, *27*, 224002.
11. Pfeiffer, C.; Emani, N.K.; Shaltout, A.M.; Boltasseva, A.; Shalaev, V.M.; Grbic, A. Efficient light bending with isotropic metamaterial Huygens' surfaces. *Nano Lett.* **2014**, *14*, 2491-2497.
12. Sautter, J.; Staude, I.; Decker, M.; Rusak, E.; Neshev, D.N.; Brener, I.; Kivshar, Y.S. Active tuning of all-dielectric metasurfaces. *ACS Nano* **2015**, *9*, 4308-4315.
13. Shalaev, M.I.; Sun, J.; Tsukernik, A.; Pandey, A.; Nikolskiy, K.; Litchinitser, N.M. High-efficiency all-dielectric metasurfaces for ultracompact beam manipulation in transmission mode. *Nano Lett.* **2015**, *15*, 6261-6266.
14. Pors, A.; Nielsen, M.G.; Della Valle, G.; Willatzen, M.; Albrektsen, O.; Bozhevolnyi, S.I. Plasmonic metamaterial wave retarders in reflection by orthogonally oriented detuned electrical dipoles. *Opt. Lett.* **2011**, *36*, 1626-1628.
15. Khorasaninejad, M.; Crozier, K.B. Silicon nanofin grating as a miniature chirality-distinguishing beam-splitter. *Nat. Commun.* **2014**, *5*, 5386.
16. Lin, D.; Fan, P.; Hasman, E.; Brongersma, M.L. Dielectric gradient metasurface optical elements. *Science* **2014**, *345*, 298-302.
17. Chen, W.T.; Khorasaninejad, M.; Zhu, A.Y.; Oh, J.; Devlin, R.C.; Zaidi, A.; Capasso, F. Generation of wavelength-independent subwavelength Bessel beams using metasurfaces. *Light: Sci. Appl.* **2017**, *6*, e16259.
18. Fan, Q.; Wang, D.; Huo, P.; Zhang, Z.; Liang, Y.; Xu, T. Autofocusing Airy beams generated by all-dielectric metasurface for visible light. *Opt. Express* **2017**, *25*, 9285-9294.
19. Song, E.Y.; Lee, G.Y.; Park, H.; Lee, K.; Kim, J.; Hong, J.; Kim H.; Lee, B. Compact Generation of Airy Beams with C-Aperture Metasurface. *Adv. Opt. Mater.* **2017**, *5*, 1601028.
20. Li, Z.; Cheng, H.; Liu, Z.; Chen, S.; Tian, J. Plasmonic airy beam generation by both phase and amplitude modulation with metasurfaces. *Adv. Opt. Mater.* **2016**, *4*, 1230-1235.
21. Zhou, J.; Liu, Y.; Ke, Y.; Luo, H.; Wen, S. Generation of Airy vortex and Airy vector beams based on the modulation of dynamic and geometric phases. *Opt. Lett.* **2015**, *40*, 3193-3196.
22. Liu, Y.; Ke, Y.; Zhou, J.; Liu, Y.; Luo, H.; Wen, S.; Fan, D. Generation of perfect vortex and vector beams based on Pancharatnam-Berry phase elements. *Sci. Rep.* **2017**, *7*, 44096.
23. Devlin, R.C.; Ambrosio, A.; Wintz, D.; Oscurato, S.L.; Zhu, A.Y.; Khorasaninejad, M.; Oh, J.; Maddalena, P.; Capasso, F. Spin-to-orbital angular momentum conversion in dielectric metasurfaces. *Opt. Express* **2017**, *25*, 377-393.
24. Aieta, F.; Genevet, P.; Kats, M.A.; Yu, N.; Blanchard, R.; Gaburro, Z.; Capasso, F. Aberration-free ultrathin flat lenses and axicons at telecom wavelengths based on plasmonic metasurfaces. *Nano Lett.* **2012**, *12*, 4932-4936.
25. Khorasaninejad, M.; Chen, W.T.; Devlin, R.C.; Oh, J.; Zhu, A Y.; Capasso, F. Metalenses at visible wavelengths: Diffraction-limited focusing and subwavelength resolution imaging. *Science* **2016**, *352*, 1190-1194.
26. Khorasaninejad, M.; Zhu, A.Y., Roques-Carmes, C.; Chen, W.T.; Oh, J.; Mishra, I.; Devlin, R.C.; Capasso, F. Polarization-insensitive metalenses at visible wavelengths. *Nano Lett.* **2016**, *16*, 7229-7234.
27. Khorasaninejad, M.; Aieta, F.; Kanhaiya, P.; Kats, M.A.; Genevet, P.; Rousso, D.; Capasso, F. Achromatic metasurface lens at telecommunication wavelengths. *Nano Lett.* **2015**, *15*, 5358-5362.
28. Aieta, F.; Kats, M. A.; Genevet, P.; Capasso, F. Multiwavelength achromatic metasurfaces by dispersive phase compensation. *Science* **2015**, *347*, 1342-1345.
29. Li, K.; Guo, Y.; Pu, M.; Li, X.; Ma, X.; Zhao, Z.; Luo, X. Dispersion controlling meta-lens at visible frequency. *Opt. Express* **2017**, *25*, 21419-21427.
30. Yang, H.; Li, G.; Cao, G.; Yu, F.; Zhao, Z.; Ou, K.; Chen, X.S.; Lu, W. High efficiency dual-wavelength achromatic metalens via cascaded dielectric metasurfaces. *Opt. Mater. Express* **2018**, *8*, 1940-1950.
31. Khorasaninejad, M.; Shi, Z.; Zhu, A.Y.; Chen, W.T.; Sanjeev, V.; Zaidi, A.; Capasso, F. Achromatic metalens over 60 nm bandwidth in the visible and metalens with reverse chromatic dispersion. *Nano Lett.* **2017**, *17*, 1819-1824.
32. Groever, B.; Chen, W.T.; Capasso, F. Meta-lens doublet in the visible region. *Nano Lett.* **2017**, *17*, 4902-4907.

33. Khorasaninejad, M.; Chen, W.T.; Oh, J.; Capasso, F. Super-dispersive off-axis meta-lenses for compact high resolution spectroscopy. *Nano Lett*. **2016**, *16*, 3732-3737.
34. Chen, W.T.; Zhu, A.Y.; Sanjeev, V.; Khorasaninejad, M.; Shi, Z.; Lee, E.; Capasso, F. A broadband achromatic metalens for focusing and imaging in the visible. *Nat. Nanotechnol*. **2018**, *13*, 220.
35. Liang, Y.; Wei, Z.; Guo, J.; Wang, F.; Meng, H.; Liu, H. Metalenses Based on Symmetric Slab Waveguide and c-TiO2: Efficient Polarization-Insensitive Focusing at Visible Wavelengths. *Nanomaterials*. **2018**, *8*, 699.
36. Devlin, R.C.; Khorasaninejad, M.; Chen, W.T.; Oh, J.; Capasso, F. Broadband high-efficiency dielectric metasurfaces for the visible spectrum. *Proc. Natl. Acad. Sci. USA* **2016**, *113*, 10473-10478.
37. Ni, X.; Kildishev, A.V.; Shalaev, V.M. Metasurface holograms for visible light. *Nat. Commun*. **2013**, *4*, 2807.
38. Zheng, G.; Mühlenbernd, H.; Kenney, M.; Li, G.; Zentgraf, T.; Zhang, S. Metasurface holograms reaching 80% efficiency. *Nat. Nanotechnol*. **2015**, *10*, 308.
39. Yang, Y.; Wang, W.; Boulesbaa, A.; Kravchenko, I.I.; Briggs, D.P.; Puretzky, A.; Geohegan, D.; Valentine, J. Nonlinear Fano-resonant dielectric metasurfaces. *Nano Lett*. **2015**, *15*, 7388-7393.
40. Grinblat, G.; Li, Y.; Nielsen, M.P.; Oulton, R.F.; Maier, S.A. Enhanced third harmonic generation in single germanium nanodisks excited at the anapole mode. *Nano Lett*. **2016**, *16*, 4635-4640.
41. Avayu, O.; Almeida, E.; Prior, Y.; Ellenbogen, T. Composite functional metasurfaces for multispectral achromatic optics. *Nat. Commun*. **2017**, *8*, 14992.
42. Wen, D.; Chen, S.; Yue, F.; Chan, K.; Chen, M.; Ardron, M.; Li, K.F.; Cheah, K.W.; Pun, E.Y.B.; Li,G.W.; Zhang, S.; Li, G. Metasurface device with helicity-dependent functionality. *Adv. Opt. Mater*. **2016**, *4*, 321-327.
43. Maguid, E.; Yulevich, I.; Veksler, D.; Kleiner, V.; Brongersma, M.L.; Hasman, E. Photonic spin-controlled multifunctional shared-aperture antenna array. *Science* **2016**, *352*, 1202-1206.
44. Khorasaninejad, M.; Chen, W.T.; Zhu, A.Y.; Oh, J.; Devlin, R.C.; Rousso, D.; Capasso, F. Multispectral chiral imaging with a metalens. *Nano Lett*. **2016**, *16*, 4595-4600.
45. Dong, H.; Wang, F.; Liang, R., Wei, Z.; Meng, H.,; Jiang, L.H.; Cen, H.; Wang, L.; Qin, S.; Wang, C. Visible-wavelength metalenses for diffraction-limited focusing of double polarization and vortex beams. *Opt. Mater. Express* **2017**, *7*, 4029-4037.
46. Shi, Z.; Khorasaninejad, M.; Huang, Y. W.; Roques-Carmes, C.; Zhu, A.Y.; Chen, W.T.; Sanjeev, V.; Ding, Z.W.; Tamagnone, M.; Chaudhary, K.; Devlin, R.C.; Qiu, C.W.; Capasso, F. Single-Layer Metasurface with Controllable Multiwavelength Functions. *Nano Lett*. **2018**, *18*, 2420-2427.
47. Arbabi, A.; Horie, Y.; Bagheri, M.; Faraon, A. Dielectric metasurfaces for complete control of phase and polarization with subwavelength spatial resolution and high transmission. *Nat. Nanotechnol*. **2015**, *10*, 937.
48. Mueller, J.B.; Rubin, N.A.; Devlin, R.C.; Groever, B.; Capasso, F. Metasurface polarization optics: independent phase control of arbitrary orthogonal states of polarization. *Phys. Rev. Lett*. **2017**, *118*, 113901.